Journal of Aerosol Science 198 (2026) 106880

Contents lists available at ScienceDirect

Journal of Aerosol Science

journal homepage: www.elsevier.com/locate/jaerosci

Deuterium analysis in cement aerosols using CF-LIBS

Aurélien Favre [a,b,*], Samuel Peillon [b], Thomas Gelain [b], Mickaël Payet [c], Arnaud Bultel [a], Élodie Bernard [d]

[a] CORIA, UMR 6614, Université de Rouen Normandie, Saint-Etienne du Rouvray, 76801, France
[b] Autorité de Sûreté Nucléaire et de Radioprotection (ASNR), DRS/SCA, Saclay, F-91400, France
[c] SCBM, CEA Saclay, Gif-sur-Yvette, 91191, France
[d] IRFM, CEA Cadarache, Saint-Paul-lez-Durance, 13108, France

ARTICLE INFO

Keywords:
Deuterium
Dismantling
Aerosol
CF-LIBS
Tritium
Particle

ABSTRACT

The operation and decommissioning of nuclear facilities, including fusion devices and advanced fission reactors, lead to the production of tritium, which can migrate through materials and be released into the environment. During maintenance and dismantling activities, tritium can become trapped in metallic or cement dusts that can be released as aerosols, raising significant safety and environmental concerns. Measuring tritium in particles remains challenging, as conventional analytical techniques require sampling and are not suitable for real-time monitoring. Laser-Induced Breakdown Spectroscopy (LIBS) offers a promising alternative by enabling direct, *in situ*, and real-time quantitative chemical analysis of aerosols. However, hydrogen isotope detection by LIBS is particularly demanding due to high excitation energy requirements, small isotopic shifts, matrix interferences, and plasma non-equilibrium effects. To address these topics, this work investigates the feasibility of detecting hydrogen isotopes embedded in cement aerosols representative of decommissioning scenarios using a calibration-free LIBS approach. Deuterium is used as a non-radioactive surrogate for tritium. The cement aerosol exhibits a median aerodynamic diameter of 5 µm and a mass concentration of (178 ± 21) mg/m^3. Under these conditions, statistical analysis indicates that a maximum of approximately 3 particles are vaporized per 100-shot acquisition. Despite this extremely low sampled mass, the deuterium signal is reliably identified and modeled, yielding a mean D/H atomic ratio of ≈ 0.26, with values ranging from ≈ 0.14 to ≈ 0.33 across acquisitions. These results demonstrate that CF-LIBS can provide quantitative isotopic information in a regime dominated by discrete particle sampling and low signal-to-background ratios, opening perspectives for real-time monitoring of tritiated aerosols in nuclear decommissioning environments.

1. Introduction

The operation of nuclear power plants and fusion devices generates tritium under high-temperature conditions (Grisolia et al., 2019). Because of its high mobility, tritium can permeate through confinement materials and potentially be released into the environment (Kim et al., 2021). In fusion facilities, tritiated metallic dusts are produced during normal operation, maintenance, and especially during dismantling and decommissioning (D&D) activities (Ashikawa et al., 2020; Bernard, Sakamoto, et al., 2019). Similar issues arise in fission plant D&D where tritium trapped in concrete or other structural materials can be released in the form of fine airborne dust (Vankrunkelsven et al., 2025). Such tritiated aerosols, including steel and cement particles, raise

* Corresponding author at: CORIA, UMR 6614, Université de Rouen Normandie, Saint-Etienne du Rouvray, 76801, France.
E-mail address: aurelien.favre@coria.fr (A. Favre).

https://doi.org/10.1016/j.jaerosci.2026.106880
Received 7 April 2026; Received in revised form 2 July 2026; Accepted 21 July 2026
Available online 28 July 2026

safety and environmental concerns due to their potential contamination (Slomberg et al., 2024). Tritium monitoring in these contexts is essential, both to assess the contamination level of materials and to evaluate the efficiency of detritiation or trapping technologies. However, measurement of tritium is challenging, especially when it is embedded in particulate matter, which can lead to an underestimation of the tritium source term (Bernard, Jambon, et al., 2019). Conventional measurement methods for tritium trapped in solids include liquid scintillation counting (El-Kharbachi et al., 2014; Sharpe et al., 2019), calorimetry technique (Bukki-Deme et al., 2013), autoradiography (Otsuka et al., 2018) and β-ray induced X-ray spectrometry (BIXS) (Matsuyama & Abe, 2016). In particular, liquid scintillation counting involves aerosol collection, sample preparation and dissolution prior to radiometric analysis, resulting in lengthy and labor-intensive procedures. These procedures become particularly challenging for heterogeneous aerosols containing micrometric or metallic particles, which may be difficult to dissolve. For example, Peillon et al. (2020) reported a 4 days dissolution time for tritiated tungsten micrometer particles. Similarly, autoradiography requires aerosol sampling, sample conditioning, exposure and image processing steps, making both techniques poorly suited for rapid monitoring of airborne radioactive particles. In practice, radioactive aerosol monitoring is mainly based on indirect techniques, such as air filtration followed by offline analysis, or on instruments measuring general aerosol properties (aerodynamic, electrical, optical, or radioactive), which generally lack chemical speciation (Vasilatou et al., 2025). Real-time aerosol measurement techniques capable of providing isotopic and chemical composition remain scarce, especially for refractory or insoluble particles.

Laser-Induced Breakdown Spectroscopy (LIBS) offers significant advantages for such applications, as it enables direct, *in situ*, and real-time chemical analysis of aerosols without the need for sample collection (Hahn & Lunden, 2000). LIBS has been successfully applied to the analysis of airborne metallic and oxide particles, both directly in the aerosol phase (Gallou et al., 2011) and indirectly after collection on filters (Marina-Montes et al., 2021). However, LIBS analysis of aerosols remains challenging because only a small fraction of laser-induced plasmas effectively interact with particles, especially under dilute aerosol conditions. Research efforts have therefore focused on improving particle sampling efficiency through various strategies. Tailored injector-extractor geometries and controlled gas flows have been shown to increase the probability of particle-plasma interactions (Lee et al., 2017). The electrostatic and electrodynamic concentration of charged particles has also been explored to allow single-particle analysis under dilute conditions (Diwakar et al., 2012). On the data-processing side, conditional analysis methods, in which only spectra corresponding to successful particle-plasma interactions are retained, have been shown to substantially improve the sensitivity of analytes (Diaz & Hahn, 2021). High-repetition-rate LIBS combined with two-dimensional spectral correlation analysis has also enabled quasi-continuous monitoring of submicrometric aerosols by significantly increasing the number of detected particle events (Xue et al., 2024). More recently, multimodal strategies combining optical emission and acoustic signatures have been proposed to improve the robustness of LIBS measurements in complex aerosol environments, and machine learning approaches have further demonstrated their ability to enhance the analytical power of such systems (Favre, Abad, et al., 2025; Liu et al., 2026; Ye et al., 2026). Direct LIBS analysis often yields lower detection limits than filter-based methods, considering that the efficiency of particle vaporization can be a limiting factor. Indeed, careful control of experimental conditions such as surrounding gas composition, laser focusing, and spectral acquisition strategy is critical for reliable quantification (Boudhib et al., 2016; Hu et al., 2022). In this context, the use of Calibration-Free LIBS (CF-LIBS) is of particular interest for complex matrices such as cement dust, where suitable reference materials are often unavailable (Favre, Bultel, et al., 2025). However, hydrogen isotope detection by LIBS faces a set of specific and interrelated challenges:

High excitation energy requirement The commonly used Balmer α transitions (H_α = 656.28 nm, D_α = 656.11 nm) require upper-level excitation energies $\geq$ 12 eV, demanding plasma electron temperatures of the order of 10^4 K or higher (Parigger et al., 2015).

Small isotopic shift The spectral separation between the H_α and D_α lines is only $\sim$ 0.17 nm. Resolving these peaks requires high-resolution spectrometers ($<$ 0.05 nm) and minimal Stark broadening, which is difficult at atmospheric pressure where collisional effects induce overlapping (Konjević et al., 2012; Paris et al., 2017).

Matrix line interference Emission from matrix elements (e.g., tungsten in fusion debris (Almaviva et al., 2021; Roldán et al., 2021) or calcium and iron in cement (Burger & Hermann, 2016)) can overlap with hydrogen isotope lines, requiring robust deconvolution procedures.

LTE assumption sensitivity CF-LIBS relies on Local Thermodynamic Equilibrium (LTE) to relate emission intensities to species concentrations. Hydrogen lines can deviate from LTE in transient plasmas, and errors in electron temperature or density estimation, derived from matrix element lines, can significantly bias hydrogen isotope quantification (Cristoforetti et al., 2010).

Self-absorption and environmental effects Balmer lines may be self-absorbed in dense plasmas, leading to underestimated concentrations (Sherbini et al., 2012). In addition, ambient humidity or adsorbed water can contribute to hydrogen signals and distorting H/D/T ratios (D'Ulivo et al., 2006; Paris et al., 2017).

Sampling variability in aerosols For airborne particles, each laser shot samples a different ensemble of particles, introducing statistical approach. This variability is exacerbated when the isotope of interest is present in trace amounts or is unevenly distributed within particles (Hahn & Lunden, 2000). In addition, heterogeneous particle laser ablation can lead to fluctuating plasma temperatures, which directly impact CF-LIBS quantification (Gallou et al., 2011).

Previous studies have shown that isotopic discrimination between hydrogen and deuterium can be achieved by LIBS under reduced pressure conditions, although spectral deconvolution is often required to resolve overlapping emission features (Favre et al., 2024). However, the direct detection of tritium remains challenging due to its radioactivity, which restricts experimental investigations and motivates the use of deuterium as a nonradioactive surrogate.

In this context, the present work investigates the feasibility of detecting deuterium incorporated into cement particles produced during cutting operations representative of decommissioning and dismantling (D&D) scenarios (Vankrunkelsven et al., 2025). By employing calibration-free LIBS (CF-LIBS), the objective is to demonstrate the capability for direct determination of the chemical composition of airborne decommissioning dust, with particular emphasis on addressing the analytical challenges associated with hydrogen isotope detection.

2. Experimental system and methodology

2.1. Technical constraints of LIBS on aerosols

Focusing an ultrashort (ns/ps) laser pulse of few mJ leads to irradiance levels high enough to induce avalanche ionization through electron cascade. The irradiance thresholds φ_{th} required for plasma formation varies with the density of the medium in which the laser pulse is focused. Typical values range from $\sim 10^{10}$ W m^{-2} to $\sim 10^{16}$ W m^{-2}. The plasma thus generated is a transient object with a lifetime $\tau_p \sim 10$ µs, characterized by steep temporal dynamics in volume V_p (few µm^3 to some mm^3), in electron density n_e ($\sim 10^{25}$ m^{-3} to $\sim 10^{20}$ m^{-3}) and in temperature T ($\sim 10^5$ K to some 10^3 K) resulting in strong gradients formation. Laser-induced breakdown spectroscopy analysis consists in performing optical emission spectroscopy on this laser-induced plasma. Depending on the focusing conditions, the surrounding environment and the observation delay, it is possible to quantify multiple elements present in the plasma.

In aerosol LIBS, the elements of interest are present in extremely small quantities within the plasma volume. At the macroscopic scale, the particles nearly do not affect ambient absorptivity. Spectroscopically, the plasma is overwhelmingly composed of atoms and ions from the ambient gas, with the radiative signature of suspended particles appearing only as trace emission lines. Accurate quantification relies on a stoichiometric relationship between the particles initially present in the plasma and those responsible for the observed emission. This requires complete sublimation of the particles in the focusing volume. This can be achieved by maximizing the specific energy delivered to each particle by utilizing high-energy pulses and by increasing the ionization threshold of the carrier gas to maximize energy transfer to the solid particles before gas breakdown occurs. Concerning diatomic carrier gas, nitrogen for instance, the process would be similar but the laser irradiance should be higher since a part of the laser energy would be devoted to N_2 dissociation. The choice of helium (monoatomic gas with the highest ionization potential of the periodic table) as carrier gas is motivated by these considerations.

From a technical point of view, operating with high-energy pulses in helium imposes specific requirements on the optical path, which must be optimized to high laser flux. The purity of helium is also important: impurities, especially metallic or oxide traces, can significantly reduce the breakdown threshold, altering the plasma formation dynamics.

In this study, the objective is to detect and quantify deuterium, used here as a surrogate of tritium, trapped in aerosol particles. Deuterium was selected as a non-radioactive surrogate for tritium to enable the development and validation of the CF-LIBS methodology under laboratory conditions without the constraints associated with radioactive materials. Although isotope effects may affect some transport or exchange processes in cementitious materials, deuterium and tritium share the same electronic structure and are incorporated into hydrated cement phases through similar chemical mechanisms. Their Balmer emission lines originate from identical atomic transitions and differ only by an isotopic wavelength shift resulting from the difference in nuclear mass. Consequently, the spectral discrimination strategy developed here for H/D mixtures is expected to be transferable to H/T systems. The objective of the present work is therefore not to reproduce the complete physicochemical behavior of tritium in cement aerosols, but rather to demonstrate the feasibility of CF-LIBS for the detection and quantification of hydrogen isotopes embedded in airborne cement particles. In the presence of hydrogen, the small isotopic shift makes spectral discrimination between H and D/T particularly challenging. It is therefore critical to minimize hydrogen contamination in the analysis chamber by controlling residual humidity and avoiding hydrogen-bearing impurities in the gas supply. Only under these conditions can the extremely unfavorable theoretical detectability thresholds for deuterium/tritium be approached, making its observation practically achievable.

2.2. Aerosol dedicated LIBS device

The dedicated aerosol LIBS device designed for this study is described in Fig. 1. The data related to this platform is gathered in Table 1. For laser safety reasons, the entire platform is equipped with an interlocked protective cover that is opaque to infrared laser pulses.

The optical laser path is detailed in Fig. 1(a) along the laser beam propagation axis indicated in green. An optical shutter (OS) synchronized with the laser source allows the desired number of pulses to be controlled and the laser breakdown frequency in the aerosol flow to be modified. Rotating a half-wave plate (HWP) coupled to a polarizing beam splitter (PBS) allows the average laser energy transmitted to the analysis system to be modified. The coupling of diverging and converging lenses is used as beam expander (BE) in order to optimize the focusing. This beam with increased diameter (expansion factor of γ depending of focal distances of used lenses) is shown in bold and propagates through a high-pass dichroic mirror (DM) whose spectral transmittance is close to unity at 1064 nm. The diameter extended beam is then focused using a plano-convex lense treated for high-flux YAG laser pulses (YAG PCL) through a high-flux window (YAG W) into the inter-nozzle space located in the middle of the LIBS analysis chamber (the aerosol path is indicated by a vertical blue arrow). In our operating conditions, the mean waist values are $\varphi_L \sim 10^{17}$ W m^{-2} and $F_L \sim 10^4$ J cm^{-2} for irradiance and fluence, respectively. The spot diameter is designed to be negligible compared to inter-nozzle distance δ_N. The Rayleigh distance is comparable to aerosol flow diameter in order to ensure an homogeneous energy deposition.

Table 1
Characteristics of the aerosol LIBS platform.

Item (Accronym)	Data	Symbol	Value
QUANTEL Briant B	Pulse wavelength	λ_L	1064 nm
	Energy	E_L	200 mJ
	Pulse duration	τ_L	6.0 ns
	Repetition rate	ν_L	10 Hz
	Quality factor	M^2	3.0
	Pulse-to-pulse stability	$\Delta E_L/E_L$	< 0.1 %
	Output beam diameter	d_L	9 mm
Beam expander (BE)	Expansion factor	γ	2
Focusing lens (YAG PCL)		f	100 mm
Aerosol flow nozzles	Inter-nozzles distance	δ_N	$1 < \delta_N(\text{mm}) < 12$
Aryelle Butterfly	Focal length	f_s	400 mm
Echelle spectrometer	Aperture	$f_s/10$	
	Slit width		50 µm
	Optical fiber bundle diameter		600 µm
	Lorentzian apparatus FWHM[a] at 700 nm		0.04 nm
	Spectral resolution at 700 nm	$\lambda/\Delta\lambda$	~ 35 000
Andor iStar DH334T camera	Pixel size		13×13 µm^2
	Quantum efficiency at 700 nm		~5 %
Palas Welas 2100	Aerosol spectrometer		0.6 – 40 µm
	Max concentration		up to 10^5 P cm^{-3}
Bronkhorst EL-Flow	Mass Flow Controller	MFC	0.16 – 8 L min^{-1}
Vortex Shaker VS-1000	Powder disperser		0.05 – 50 µm
	Volumetric flow rate		1 – 5 L min^{-1}

[a] Full Width at Half Maximum.

The C22 alloy used for the LIBS chamber allows acid rinsing in the event of tritiated particle deposits. Downstream from the focal point, the laser energy at the chamber outlet is transmitted by a second DM towards a beam dump (BD) and a fast camera to monitor the inter-nozzle alignment. The laser-induced plasma radiates in all directions (4π sr). The geometry of the chamber only allows this emission to be exploited in the two directions indicated in red. The plasma radiation is retro-collected and reflected by the first DM in order to be focused towards a bundle of optical fibers connected to a spectroscopic acquisition device. The height of the chamber can be adjusted using a dedicated stand and its position can be adjusted using micro-controlled stages. This technical choice makes it possible to secure all the optical axes together and thus perform a single adjustment in order to avoid any laser damage to the nozzles. Once the aerosol flow is operational, no adjustment is possible and no visual inspection is possible perpendicular to the laser optical axis.

Concerning the aerosol flow axis, details are given in Fig. 1(b). Pure bottled helium is used and is first sent to a filtration and drying unit and then to a pressure regulator set at 1 bar. The gas then passes through a flow splitter which distributes it to two Bronkhorst EL-FLOW mass flow controller (MFCs) factory-calibrated for helium in the range of $0.16 - 8$ L min^{-1}. The first MFC supplies the Vortex Shaker (powder disperser device, patent EP2794117B1 by Roynette and Gensdarmes 2012) with a constant flow rate Q_a. The second MFC supplies the aerosol injection nozzle with annular flushing gas Q_s. The particles resuspended in the Vortex Shaker are drawn towards the injection nozzle, which is installed in the LIBS chamber perpendicular to the laser beam path. The aerosol passes through the chamber and is collected by a collection nozzle with an inlet diameter of 4 mm. The aerosol is then transported to a Palas Welas 2100 optical counter which measures the concentration and particle number distribution of the aerosol. At the device's outlet, a collection filter (47 mm diameter) is weighed before and after each experiment to determine the average mass concentration of the aerosol during each test.

After numerous empirical tests, a standardized particle resuspension protocol ensuring a consistent and steady particle concentration in the inter-nozzle volume has been identified. The best results (controlled LIBS diagnostic with minimal mass fluctuations in the plasma volume) are obtained with the following steps:

- the Vortex Shaker bucket is filled with a mass m_p of particles to be resuspended and a mass $3m_p$ of bronze particles ($d_{50} \approx 150$ µm) used as mechanical mixers,
- the mechanical agitation frequency is set,
- the total carrier gas flow $Q_t = Q_a + Q_s$ is linearly increased using the calibrated MFCs,
- when $Q = Q_t$, a characteristic time τ_a to approach aerosol flow steady state is observed before starting the LIBS diagnostic.

This experimental protocol is used for every experimental results presented in this paper.

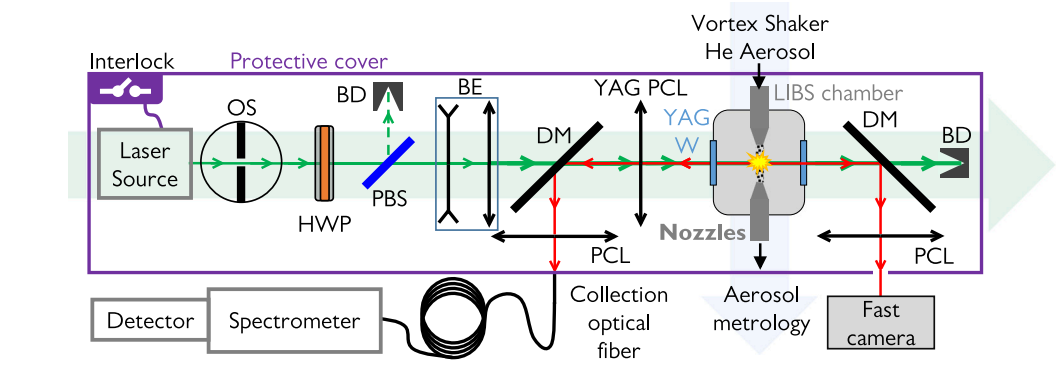

(a) **Laser path** (horizontal green arrow). The beam from the laser source (in green) is extended by a beam expander, passes through a dichroic mirror and is focused by a YAG plano-convex lens in the inter-nozzle space of the LIBS chamber. The laser-induced plasma (in yellow) emits its light (in red). A part of this light is reflected and focused to an optical fiber bundle towards the spectrometer for analysis.

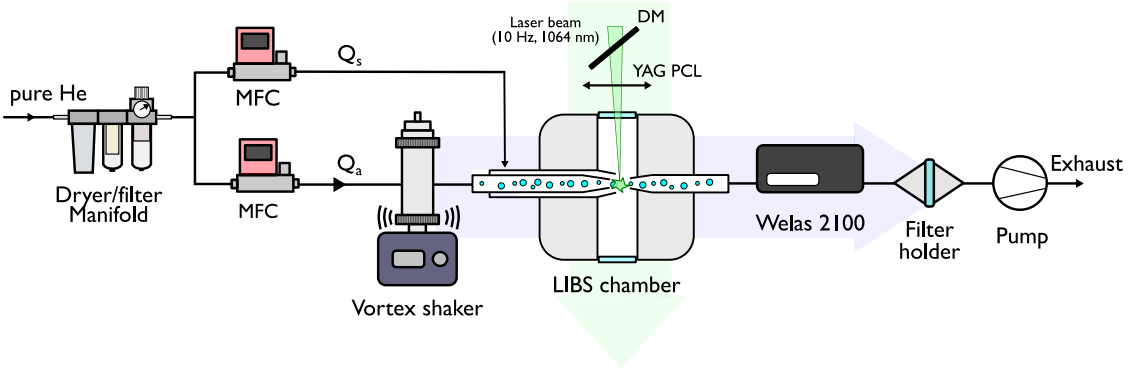

(b) **Aerosol path** (horizontal blue arrow). Helium gas passes through a flow splitter which distributes it to two mass flow controller (MFCs) factory-calibrated for helium. The first MFC supplies the Vortex Shaker with a constant flow rate Q_a. The second MFC supplies the aerosol injection nozzle with annular flushing gas Q_s. The particles suspended in the Vortex Shaker are then drawn towards the injection nozzle, which is installed in the LIBS chamber perpendicular to the laser beam path. The aerosol passes through the chamber and is collected by another nozzle sending the aerosol to a Palas Welas 2100 optical counter for analysis.

Fig. 1. Schematic view of the aerosol LIBS platform.

2.3. Plasma geometry, particles transport and laser interaction

The plasma geometry is considered as cylindrical as depicted on Fig. 2a. The coaxial plasma dimension ℓ_p is evaluated from the length $\ell_{He} = \Delta z$ estimated from Gaussian irradiance calculations predicting $\varphi_L(z \in [-\frac{\ell_{He}}{2}, \frac{\ell_{He}}{2}]) \geq \varphi_{th,He}$ with $\varphi_{th,He}$ the irradiance threshold of helium. For infrared nanosecond laser pulses, the helium breakdown threshold is considered to be $\varphi_{th,He} = 5 \times 10^{15}$ W m^{-2} according to the works of Evans and Gamal (1980), Morgan et al. (1971) and Turcu et al. (1997). As a result in our focusing conditions, the corresponding value of ℓ_{He} is close to 4 mm. The value of ℓ_{He} is then spectroscopically adjusted using an iterative method to estimate ℓ_p. In our case, the correction between ℓ_{He} and ℓ_p allowing satisfactory emission spectra simulations does not exceed 40% for early plasma expansion. The mean plasma diameter (radial plasma dimension) can be directly measured using co-axial imaging allowing the evaluation of the plasma volume V_p.

In order to maximize the aerosol concentration in the plasma volume, a specific injection nozzle incorporating an annular flow promoting the guidance and therefore the rectilinear path of the resuspended particles was designed based on previous work (Lee et al., 2017; Park et al., 2009). This system, coupled with a collection nozzle, makes it possible to significantly limit the formation of turbulence which could lead to the deposition of particles on the windows. In order to simplify the protocol leading to the steady state aerosol flow regime, a computational fluid dynamics (CFD) investigation (not exposed here) helped to determine the minimal aerosol flow rate $Q_{a,min}$ allowing to operate without annular sheath flow. These numerical simulations were performed for both polydisperse and monodisperse aerosol distributions, showing no significant variation in the inter-nozzle average velocity. CFD simulations representative of the physical situation are presented in Fig. 2b considering a monodisperse aerosol with a geometric median diameter of the particles transported in helium set to 5 μm. These calculations are carried out in Lagrangian using a total helium flow rate of $Q_t = Q_a + Q_s$, with $Q_a = 4$ L min^{-1} $> Q_{a,min}$ the aerosol flow rate and $Q_s = 0$ L min^{-1} the annular sheath flow rate (not necessary in this flow configuration). We note that the geometry of the injection nozzle (upper part of the illustrations in

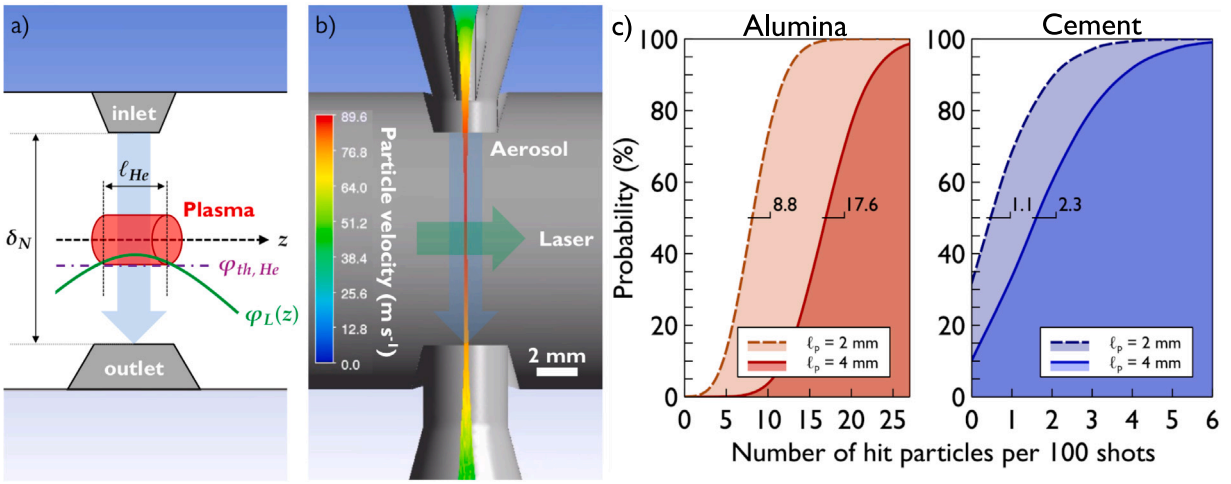

Fig. 2. **a**: Plasma geometry within the inter-nozzle space in which aerosol flows.
b: Lagrangian CFD simulations of the transport of the aerosol: average inter-nozzle velocity projection ~80 m s^{-1}.
c: Poisson sampling probability for Al_2O_3 (left) and cement (right).

Fig. 2b) ensures a rectilinear trajectory of the aerosol flow towards the collection nozzle. In the context of these simulations, the chamber geometry corresponds to the LIBS experimental setup. The laser optical axis is therefore represented by a cylinder with a diameter of 14 mm and a length of 90 mm, oriented perpendicular to the aerosol flow axis. The internal chamber volume is sufficiently large to prevent wall effects (near-zero average velocity outside the inter-nozzle region). As for experiments, the inter-nozzle distance is set to $\delta_N = 10$ mm. Experimentally, this distance can still be reasonably reduced while avoiding plasma-nozzle contact since the plasma diameter is smaller than 2 mm in our focusing conditions. The inter-nozzle velocity field presents satisfactory uniformity with an average inter-nozzle flow velocity of ~80 m s^{-1} and an average particle concentration of some 10^7 particle m^{-3} (particles are assumed to be monodisperse and spherical) into a ~ 100 μm wide particles jet. Considering this physical situation, both characteristic plasma lifetime $\tau_p = 10$ μs and average particle residence time in the inter-nozzle space ($\sim 10\tau_p$) are negligible compared to inter-pulse delay (100 ms). This prevents any multiple laser-matter interaction for a given particle probed.

In terms of monitoring laser-particle interaction, the monodisperse approach cannot be considered. In fact, due to the finite volume of LIBS plasma and the discrete nature of the particles constituting the aerosol, a complex sampling problem arises (Diwakar et al., 2012). For each plasma event, the sampling volume is considered unchanged. This assumption is reasonable since the aerosol LIBS analysis is operated in steady state flow with a satisfactory pulse-to-pulse energy stability. This technique was developed and discussed in detail in previous work by Hahn (1998). In particular, discrete aerosol sampling by LIBS can be modeled using Poisson statistics where

$$P_n = \frac{\mu^n}{n!} e^{-\mu} \tag{1}$$

is the probability of sampling n particles in a given plasma volume. In Eq. (1), n is an integer and μ is the average number of particles per plasma volume, namely,

$$\mu = C_n \times V_p \tag{2}$$

easily calculated as the product of the particle number per unit volume of gas, C_n, and the effective plasma sampling volume, V_p. The particle volume concentration in the inter-nozzle volume is obtained by dividing the particle flux by the volume swept by the particles each second, multiplied by the particle velocity in the inter-nozzle volume. Considering that the particle jet is contained within a cylinder whose diameter is equivalent to the diameter of the injection nozzle (1 mm), then in our conditions $C_n \sim 10^7$ m^{-3}. Thus, we find that the average number of particles concentration per plasma volume for each laser shot is $\sim 10^{-2}$ particles per shot. This quantity can also be called the "particle hit rate" or the vaporization/dissociation rate of particles for each laser shot. When this value is much less than one, it implies a low sampling rate, meaning that a positive spectral signal (including an emission line from the material constituting the particles) corresponds to a single particle in the plasma volume. The sampling frequency is then approximated by this quantity (Hahn et al., 1997). The cumulated sampling probabilities as a function of the number of vaporized particles calculated with Eq. (1) are presented in Fig. 2c for Al_2O_3 (left) and cement (right) experiments. For the tests with alumina particles, we calculated that the average number of particles present in the plasma volume for each laser shot is 0.088 which translates to a ~ 50 % probability of vaporizing 8.8 particle for every accumulation of 100 shots. For this calculation, the plasma diameter and length are both set to 2 mm. If we increase its length to 4 mm, it is expected to have a ~ 50 % probability of vaporizing 17.6 particles after a 100 shots accumulation. The same analysis can be performed for the experiments with cement particles. Since the particle concentration of cement aerosol is almost three times lower than that of alumina, the plasma volume is reduced with

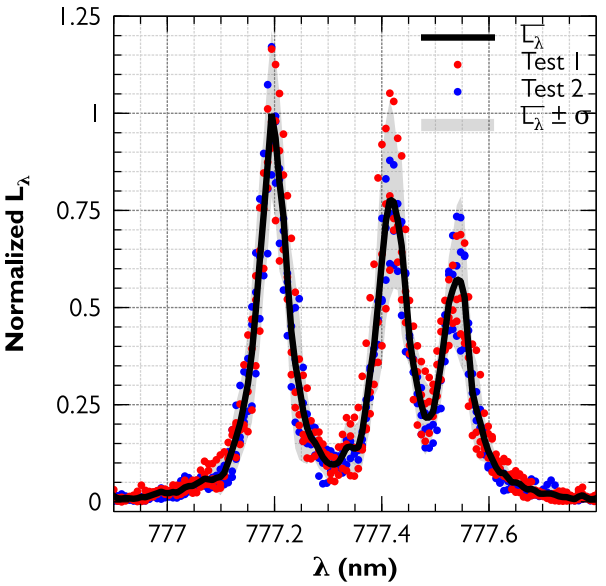

Fig. 3. Spectroscopic repeatability obtained with Al_2O_3+He aerosol (Q_a = 4 L min^{-1}, τ_p = 2 µs). The low standard deviation demonstrates a reliable protocol with steady aerosol concentration: plasma parameters (n_e, T) remain stable over an important number of vaporization events.

a plasma diameter of 1.2 mm and a length of 2 mm or 4 mm. For these two plasma geometries, one finds a ∼ 50 % probability of vaporizing 1.1 or 2.3 particles, respectively. For the cement case with a plasma length of 2 mm, it can also be seen that there is a ∼ 30 % probability of hitting zero particles even after 100 laser pulses. This probability drops to ∼ 10 % when the plasma length considered is 4 mm. These calculations demonstrate the difficulty of LIBS measurement on aerosols in the study's configuration by highlighting the discrete nature of the problem and the spectroscopic sensitivity required to identify traces of hydrogen isotopes present in the particles. The following paragraphs therefore focus on demonstrating the repeatability of the spectroscopic analysis as well as the robustness of the results obtained.

2.4. Protocol validation

In this section, we briefly present the preliminary measurements carried out to test the experimental protocol. These tests are performed with a calibrated alumina powder (DURAMAX SPM102), with a particle aerodynamic median diameter d_{50} = (6.12 ± 1.57) µm. The particles are resuspended according to the protocol described in Section 2.2. For the test conditions (Q_t = Q_a = 4 L min^{-1}, δ_N = 10 mm), we obtain $\tau_a \approx 10^2$ s. For $t > \tau_a$, the average particle concentration in the inter-nozzle volume measured by the Palas Welas 2100 is ∼900 particles s^{-1} and the mass concentration determined by filter weighting is (1325 ± 142) mg m^{-3}.

Spectroscopic repeatability

In addition to aerosol metrology measurements, the emission of laser-induced plasma generated from alumina particles aerosolized in helium was monitored during two types of measurements:

- The test N°1 consisted in generating the alumina aerosol and performing several acquisitions without interrupting the flow. This allowed to verify that the aerosol flow does not exhibit any temporal drift in terms of concentration nor particle number.
- The test N°2 involved repeating the resuspension protocol several times and performing one acquisition for each repetition. This allowed to verify the robustness of the established protocol.

For all of these acquisitions, each resulting from 100 spectral accumulations, we focused in the emission of the atomic oxygen triplet around 777 nm (see Table 2) by observing the plasma at t_p = 2 µs (with an integration window of 100 ns) in the recombination dynamics. This triplet is interesting because it allows the monitoring of fluctuations both in n_e and T. Indeed, n_e is driving triplet overlapping by Stark broadening and T values govern the density in neutral oxygen. The line ratios of this triplet also allow to decide on the achievement of the physico-chemical equilibrium of the laser-induced plasma. In fact, the achievement of local thermodynamic equilibrium is mandatory to perform a CF-LIBS quantification. Self-absorption is here excluded given the very low quantities of oxygen within the plasma. Tests N°1 and N°2 are presented in Fig. 3 by red and blue dots, respectively. The results exhibit a satisfactory repeatability on each test meaning that the adopted protocol is reliable with no temporal drift. From a more general point of view, tests N°1 and N°2 are well correlated allowing to compile statistics to obtain a mean spectrum (black solid line, used as normalization factor) framed by its standard deviation (in gray).

Table 2
Spectroscopic data used for Al_2O_3+He aerosol CF-LIBS diagnostic.

Element	λ_{ki} (nm)	A_{ki} (10^7 s^{-1})	E_i (eV)	E_k (eV)	g_i	g_k	Ref.
H I	656.28	6.46	10.199	12.087	4	6	Kramida et al. (2025), Mijatovic et al. (2020)
He I	667.81	6.37	21.218	23.074	3	5	Konjevic et al. (2002), Kramida et al. (2025)
Al II	704.21	5.78	11.316	13.077	3	5	Cirisan et al. (2014), Kramida et al. (2025)
Al II	705.66	5.74	11.316	13.073	3	3	Cirisan et al. (2014), Kramida et al. (2025)
Al II	706.36	5.73	11.316	13.071	3	1	Cirisan et al. (2014), Kramida et al. (2025)
He I	706.52	1.55	20.964	22.718	5	3	Konjevic et al. (2002), Kramida et al. (2025)
He I	728.13	1.83	21.218	22.920	3	1	Konjevic et al. (2002), Kramida et al. (2025)
Al II	747.14	5.57	13.649	15.308	5	7	Cirisan et al. (2014), Kramida et al. (2025)
O I	777.19	3.69	9.146	10.741	5	7	Gosse et al. (2025), Kramida et al. (2025)
O I	777.42	3.69	9.146	10.740	5	5	Gosse et al. (2025), Kramida et al. (2025)
O I	777.54	3.69	9.146	10.740	5	3	Gosse et al. (2025), Kramida et al. (2025)

Table 3
Detailed values associated with MERLIN simulations presented in Fig. 4.

t_p (10^{-6} s)	n_e (10^{21} m^{-3})	T (10^3 K)	ℓ_p (10^{-3} m)	x_{Al}/x_O	$(x_{Al}+x_O)/x_{He}$
1	1.00	10.20	2.50	0.695	$\approx 10^{-5}$
2	0.50	9.7	2.75	0.471	$\approx 5\times10^{-6}$
5	0.15	9.3	3.00	0.176	$\approx 2\times10^{-6}$

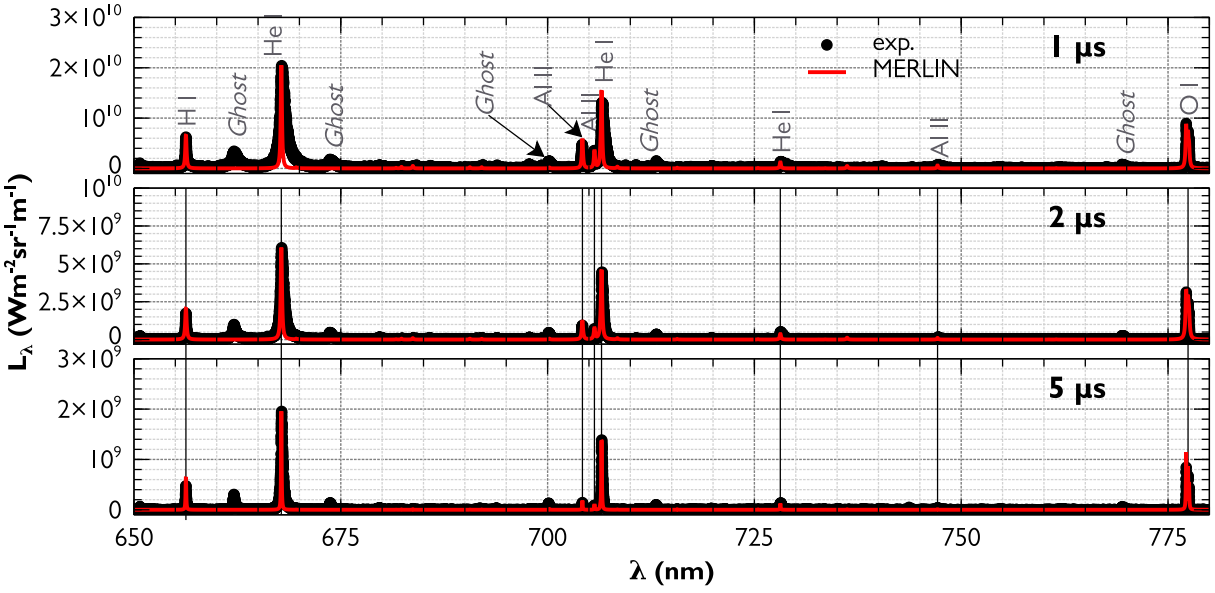

Fig. 4. Comparison of experimental spectra (in black) and simulated spectra (in red) over the spectral interval [650, 780] nm at times t_p = 1, 2 and 5 µs for an (Al_2O_3+He) aerosol laser-induced plasma.

CF-LIBS reliability

The studied emission lines used for calculations are listed in Table 2 and the Stark broadening parameters are found in the references. The electron density n_e is measured from the Stark broadening of the H_α transition at 656.28 nm. The value obtained is consolidated by modeling the O I triplet around 777.42 nm. The temperature T is evaluated using the He I/Al II line ratios and is consolidated by exploiting the He I 667.81 / He I 706.52 and Al II 704.21 / Al II 747.14 line ratios. These two ratios involve transitions whose upper levels E_k differ by several eV, which induces satisfactory temperature sensitivity. Furthermore, the large difference between the ionization potentials of He, Al and O also induces a satisfactory temperature sensitivity. The mole fractions x_i are thus determined by reconstructing the experimental spectrum using the MERLIN simulation code (Favre, Bultel, et al., 2025). Considering a mixture (x_{Al}, x_O, x_H, x_{He}), the obtained results are presented in Table 3 and depicted in Fig. 4.

Analyzing Fig. 4, one can notice the presence of ghost lines associated with the Echelle spectrometer used for the acquisition. These ghost lines do not interfere with the studied physical lines but helium lines appear to be strongly Stark shifted which complicates the simulation of time integrated spectra. Since the main scope of these simulations is the estimation of x_{Al}/x_O, no

Table 4
Elemental mass composition of the studied deuterated cement (by XRF, approximated to 10^{-4}).

Species	Na	Mg	Al	Si	P	K
y_i (%)	0.0667	0.4240	2.0714	12.5058	0.0421	0.1817
Δy_i (%)	0.0291	0.0454	0.0705	0.0848	0.0230	0.0070
Species	Ca	Ti	Mn	Fe	O	H+D
y_i (%)	37.0505	0.0896	0.0281	1.7730	20.2940	Balance
Δy_i (%)	0.2541	0.0022	0.0003	0.0185	10.8614	–

further investigation has been led regarding He simulation. The mean plasma diameter is observed to be ~ 2 mm giving a plasma volume $V_p \sim 10^{-8}$ m^{-3}. The mixture, considered in the measured thermodynamical conditions, involves a plasma pressure of $\sim 10^7$ Pa. The rather low n_e values are explained by the high ionization potential of He which is the main plasma element. The alumina stoichiometric ratio is well described for $t_p \ll \tau_p$. For longer times, dilution effects induce departure from stoichiometry. Neglecting hydrogen content ($x_H \sim 10^{-6}$), the ratios $x_{Al_2O_3}/x_{He}$ are close to 10^{-5} which is consistent with CFD calculations and well correlated with the mass concentration value measured by filter weighting.

3. Results and discussion

3.1. Description of cement sample

The deuterated cement sample was manufactured from 300 g of CEM I Portland cement mixed with deuterated water (99%) at a controlled liquid-to-solid ratio of 0.5. The resulting paste was cast into standardized molds ($20.5 \times 2 \times 8.5$ cm^3) and cured for 28 days inside a glove box. To generate aerosols, the cement plate was cut with a grinder inside a dedicated 250 L plexiglas glovebox equipped with a HEPA-filtered air inlet. The extraction flow rate was maintained at 183 ± 5 L/min throughout the experiments. Particle collection and characterization were then performed using complementary aerosol diagnostics, including an Andersen impactor (28 L/min) for aerodynamic size distribution measurements, a cyclone for bulk particle collection, and a nephelometer (DustTrak II 8530, TSI) for aerosol mass concentration monitoring. Elemental composition of the sample has been preliminary determined by XRF (X-ray Fluorescence). The XRF protocol is only sensitive to oxides and does not allow the description of light elements such as H and D. Thus, among the mass fractions of Table 4, the mass fraction y_O corresponds to the contribution deduced (not measured) from the oxygen contained in the probed oxides. Therefore, y_O is an underestimation of oxygen mole fraction contained in the cement. The complement to these values ($1 - \sum_i y_i \approx 25\%$, called fire loss) thus corresponds to an overestimation of the quantity of H and D. For CF-LIBS deuterium quantification, this XRF preliminary inventory is used as a variable reduction since only O, H and D are considered as elements to be spectroscopically quantified.

3.2. Particle size distribution and number concentration

From the solid block of deuterated cement described in Section 3.1, 0.8 g of powder were produced by cutting the solid block using an angle grinder in a suitable enclosure. The aerodynamic particle size distribution (PSD) obtained by an Andersen impactor during the particle production phase is depicted in Fig. 5(a). It can be described by a log-normal distribution with a median diameter of 5 μm and a geometric standard deviation (GSD) of 1.84. Fig. 5(b) presents the temporal monitoring by optical counting with the Welas 2100 associated with the resuspension by the Vortex Shaker. The average sampling is (324 ± 34) particle s^{-1} (red curve averaged over the yellow indicated abscissa).

Resuspension of this powder following the protocol described in Section 2.2 allows obtaining an aerosol mass concentration of (178 ± 21) mg m^{-3}.

3.3. CF-LIBS analysis on deuterated cement aerosols

The low quantity of cement powder generated by cutting did not allow us to operate several preliminary LIBS acquisition tests. Since then, prior to any aerosol measurement, the emission dynamics of the Balmer-α lines have been studied on bulk cement. The usual laser-induced plasma recombination dynamics have been observed and is not presented here. Yet, we remind that the emission of Balmer-α lines are related to electron density n_e and LTE temperature T. For a plasma generated in a high ionization potential carrier gas (such as He), n_e is mainly driven by particles compounds ionization. Generally speaking, n_e and T are coupled such as low electron densities are associated to low LTE temperatures. That being said, if T is too high, this is inducing a strong ionization of H or D which leads to low H/H^+ or D/D^+ ratios. Since protons do not spectrally radiates, high T involve a diminution of Balmer-α emission. In addition, since high T are associated with high n_e, this is inducing strong Stark broadening and shift preventing quantitative approach. The temporal window selected in the article has been chosen from a whole bench of empirical tests as the best compromise for the couple (n_e, T) to analyze Balmer-α emission. These preliminary experiments allowed the identification of a satisfactory time integration window favorable to the aerosol phase acquisition. The acquisition parameters chosen for the aerosol experiment are: 100 accumulations at $t_p = 6.5$ μs with an integration window of 100 ns. Taking into consideration the sampling calculations of Section 2.3 and the particles number measurements of Fig. 5(b),

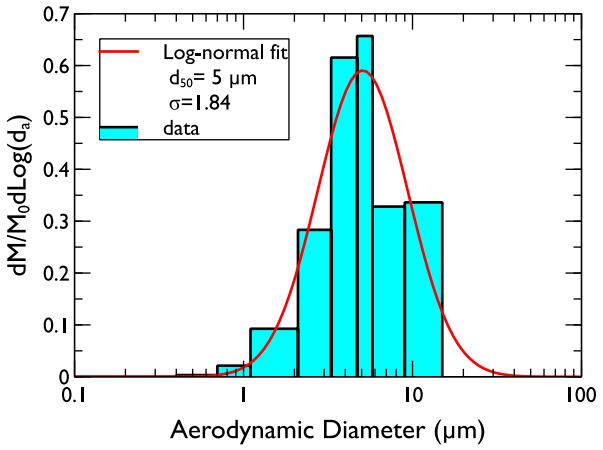

(a) Particle size distribution obtained with the Andersen impactor. The log-normal distribution exhibit a median aerodynamic diameter of 5 µm.

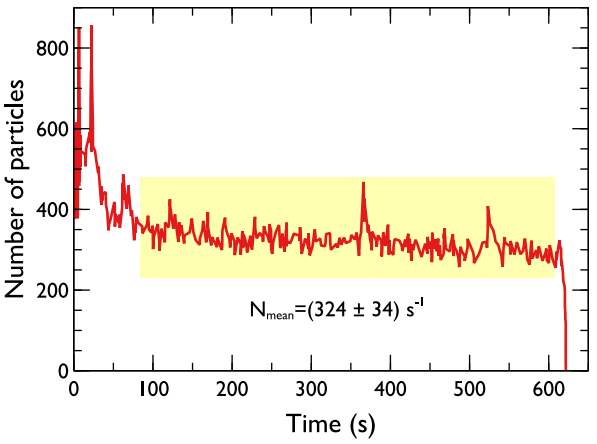

(b) Evolution of the particle number concentration generated by the Vortex Shaker and measured by the Welas 2100 aerosol spectrometer.

Fig. 5. Particle size distribution and number concentration of the deuterated cement powder resuspended with $Q_t = Q_a = 4$ L min^{-1} of He.

Table 5
Spectroscopic data used for deuterated cement+He aerosol CF-LIBS diagnostic. For cement compounds (in blue), the Stark broadening parameters are determined according to a polynomial correlation (Fantoni et al., 2017).

Element	λ_{ki} (nm)	A_{ki} (10^7 s^{-1})	E_i (eV)	E_k (eV)	g_i	g_k	Ref.
Fe I	248.33	48.0	0.000	4.991	9	11	Fantoni et al. (2017), Kramida et al. (2025)
P I	253.56	9.50	2.324	7.213	4	4	Fantoni et al. (2017), Kramida et al. (2025)
Mn II	257.51	28.0	0.000	4.811	7	9	Fantoni et al. (2017), Kramida et al. (2025)
Mg I	285.21	49.1	0.000	4.346	1	3	Fantoni et al. (2017), Kramida et al. (2025)
Si I	288.16	21.8	0.781	5.082	5	3	Fantoni et al. (2017), Kramida et al. (2025)
Ti II	334.94	16.8	0.049	3.749	10	12	Fantoni et al. (2017), Kramida et al. (2025)
Al I	394.40	4.99	0.000	3.143	2	2	Fantoni et al. (2017), Kramida et al. (2025)
Al I	396.15	9.85	0.014	3.143	4	2	Fantoni et al. (2017), Kramida et al. (2025)
Cu I	510.55	0.20	1.389	3.817	6	4	Fantoni et al. (2017), Kramida et al. (2025)
Cu I	515.32	6.00	3.786	6.191	2	4	Fantoni et al. (2017), Kramida et al. (2025)
Cu I	521.82	7.50	3.817	6.192	4	6	Fantoni et al. (2017), Kramida et al. (2025)
Na I	588.99	6.16	0.000	2.104	2	4	Fantoni et al. (2017), Kramida et al. (2025)
Na I	589.59	6.14	0.000	2.102	2	2	Fantoni et al. (2017), Kramida et al. (2025)
Ca I	643.91	5.30	2.526	4.451	7	9	Fantoni et al. (2017), Kramida et al. (2025)
Ca I	646.26	4.70	2.523	4.441	5	7	Fantoni et al. (2017), Kramida et al. (2025)
D I	656.11	6.47	10.202	12.091	4	6	Kramida et al. (2025), Mijatovic et al. (2020)
H I	656.28	6.46	10.199	12.087	4	6	Kramida et al. (2025), Mijatovic et al. (2020)
He I	667.81	6.37	21.218	23.074	3	5	Konjevic et al. (2002), Kramida et al. (2025)
K I	766.50	3.78	0.000	1.617	2	4	Fantoni et al. (2017), Kramida et al. (2025)
K I	769.90	3.73	0.000	1.610	2	2	Fantoni et al. (2017), Kramida et al. (2025)
O I	777.19	3.69	9.146	10.741	5	7	Gosse et al. (2025), Kramida et al. (2025)
O I	777.42	3.69	9.146	10.740	5	5	Gosse et al. (2025), Kramida et al. (2025)
O I	777.54	3.69	9.146	10.740	5	3	Gosse et al. (2025), Kramida et al. (2025)

these 10-second LIBS accumulations therefore correspond to the vaporization of a maximum of ~3 particles. Considering spherical cement particles with the measured median diameter of 5 µm and a density of ~2 g cm^{-3}, the total vaporized mass is thus estimated to $\sim 4\times10^{-13}$ kg. Using the experimental setup coupled with the resuspension protocol described in Section 2.2 and considering the statistical reliability described in Section 2.4, the average emission spectrum obtained from 8 different acquisitions is presented in Fig. 6. The [200, 800] nm broadband spectrum is shown in Fig. 6(a). The calibration in spectral radiance is ensured by a stabilized D_2 arc lamp for [200,400] nm range and by a W ribbon lamp for [400,800] nm range. This spectrum of deuterated cement particles resuspended in helium exhibits more than 3000 lines. The main identified lines are listed in Table 5. Every single XRF measured element is observed on LIBS spectrum: those elements are highlighted in blue. The bronze particles used as mechanical mixers for resuspension are not transported in the aerosol flow since no Cu lines is detected (indicated in red). The main helium (carrier gas) lines are indicated in orange. A focus on main cement compounds (Ca and O) as well as Cu and He radiative signature is shown on Fig. 6(b).

The emission of Balmer-α lines is highlighted in green. In order to quantify D as accurately as possible, we limit the number of free parameters for the simulation. Since then, the mass concentration is fixed to the measured value: (178 ± 21) mg m^{-3}. As

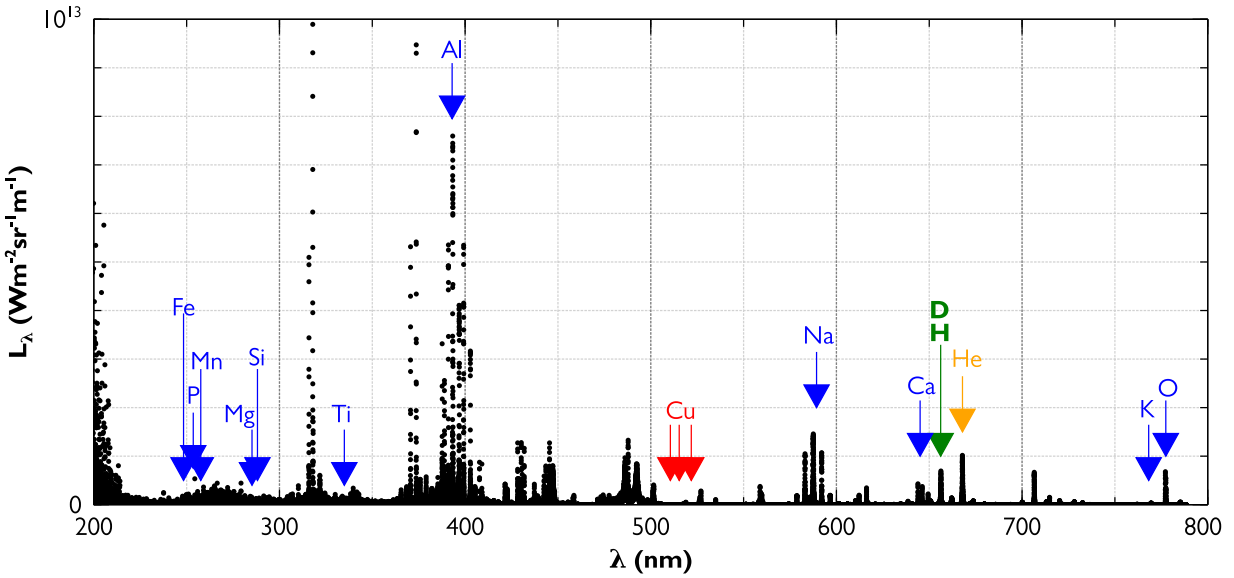

(a) Radiative signature collected over [200, 800] nm. Every component quantified by XRF are spectrally identified by LIBS (see Table 4).

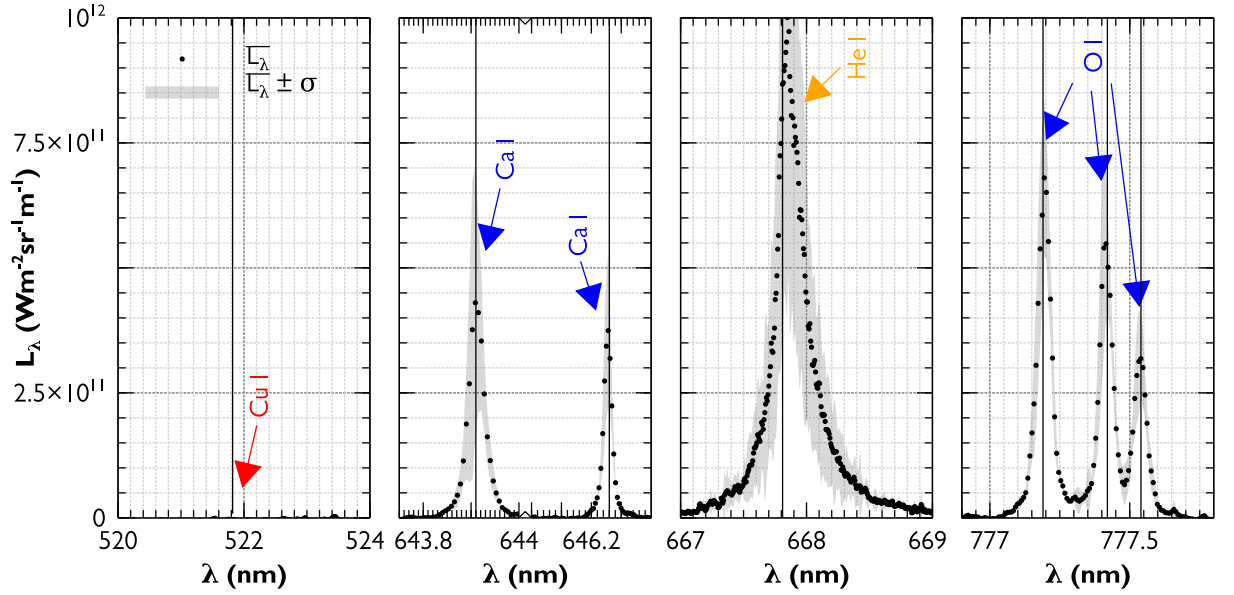

(b) Focus on Cu (mechanical resuspender), Ca (cement component), He (carrier gas) and O (cement component) emission from Fig. 6(a) with associated fluctuations.

Fig. 6. Experimental emission observed at $t_p = 6.5$ µs for a deuterated cement laser-induced plasma ($Q_t = Q_a = 4$ L min^{-1} He).

for alumina, the plasma geometry is considered cylindrical. Since it cannot be determined experimentally, and given the low mass concentration, the coaxial plasma length is taken as $\ell_p = \ell_{He} = 4.0$ mm. The plasma volume is estimated to be $\sim 5 \times 10^{-9}$ m^3. Compared to alumina aerosol plasma volume detailed in Section 2.4, this value appears to be slightly lower. This is explained by the lower mass concentration of resuspended cement particles. The measurements of mass concentration and plasma volume allow the deduction of the carrier gas quantity (here, $\sim 10^{-6}$ mg of cement particles in the plasma volume). The electron density is determined from the deconvoluted emission of H_α by considering identical Stark broadening for H and D Balmer-α lines. The measured value is found to be $n_e = 6 \times 10^{21}$ m^{-3}. This rather low electron density facilitates line identification since it induces negligible Stark shift for Balmer-α emission (Büscher et al., 2002). The temperature $T = 12.55 \times 10^3$ K is determined from an iterative procedure. Compared to the alumina experiments presented in Section 2.4, a higher temperature is measured at longer plasma observation time. This is mainly explained by the difference in aerosol concentration which is ~10 times lower for cement

Table 6
CF-LIBS composition determined by the spectral simulations of Fig. 7: x_i^* stands for mole fraction within the cement aerosol.

Min simulation				
Species	He	H	D	O, Na, Mg, Al, Si, P, K, Ca, Ti, Mn, Fe
x_i (‰)	999.68	0.076	0.011	
x_i^* (%)	–	29.71	4.13	Balance (see Table 4)
Mean simulation				
Species	He	H	D	O, Na, Mg, Al, Si, P, K, Ca, Ti, Mn, Fe
x_i (‰)	999.68	0.12	0.032	
x_i^* (%)	–	38.54	9.98	Balance (see Table 4)
Max simulation				
Species	He	H	D	O, Na, Mg, Al, Si, P, K, Ca, Ti, Mn, Fe
x_i (‰)	999.68	0.15	0.049	
x_i^* (%)	–	41.49	13.64	Balance (see Table 4)

experiments. In fact, the lower the concentration of the particles, the lower the energy required to vaporize the particles. This leads to a higher plasma temperature mainly driven by helium breakdown (the presence of particles acts as helium plasma tempering). Further information about the influence of aerosol concentration over plasma temperature can be found in the works of Asgill et al. (2015), Dalyander et al. (2008), Diaz and Hahn (2021) and Diwakar et al. (2007). Concerning the plasma composition, the measured XRF (Table 4) values are coupled with He content considering O as adjusting compound since it not directly measured by XRF. This procedure allows to use y_D and y_H as the only variables for the simulation. The detailed comparison between experimental and simulated spectra is given on Fig. 7. Following a statistical approach, one can observe fluctuations in the particle diameter from one 10-seconds acquisition to the next (corresponding to approximately one vaporized particle; see Fig. 2), as the collected signal may vary between acquisitions (the blue spectrum corresponds to a smaller particle diameter, whereas the orange spectrum corresponds to a larger one). Nevertheless, the spectral radiance ratio associated with D and H emission remains unaffected by these particle-size fluctuations. This behavior can be explained by the homogeneous deuterium concentration within the bulk deuterated cement prior to powder preparation. As a consequence, three different simulations are proposed to reconstruct the minimum (long red dashed line), the maximum (short red dashed line), and the mean (solid red) observed signals. The values obtained from the simulations (CF-LIBS measurements) are given in Table 6.

The spectroscopic analysis is particularly demanding regarding the numerous elements considered in the plasma. Among the main lines which may interfere with the Balmer-α emission, we notice the transition Si I 656.05 nm (experimentally and numerically not observed in our conditions). Likewise, many Fe, Ti and Ca lines are listed in spectroscopic database but are not observed in our conditions. Among these numerous lines, Fe I 656.92 nm and Ca I 657.28 nm appear to be the strongest expected lines. The lack of Stark broadening parameters for these two lines may explain the simulation poor quality on the range [656.35, 656.60] nm. Nevertheless, the envelope is generally well described given the very small quantities involved. For the mean simulation, the mole fractions within the plasma volume are $x_{\mathrm{D}} \sim 30$ ppm and $x_{\mathrm{H}} \sim 3x_{\mathrm{D}}$. This corresponds to an averaged deuterium vaporized mass of the order of $m_D \sim 10^{-14}$ kg. It is therefore possible to derive an estimation of the corresponding activity of tritium by calculating the mass activity of tritium $a_{T,m}$ using its molar mass $M_T = 3.016 \times 10^{-3}$ kg mol^{-1}, its specific activity $a_T = 1.9 \times 10^{-9}$ Bq atom^{-1} and the Avogadro number $N_A = 6.022 \times 10^{23}$ mol^{-1}:

$$a_{T,m} = \frac{a_T N_A}{M_T} \approx 4 \times 10^{17} \text{ Bq kg}^{-1} \tag{3}$$

This equivalent mass in tritium would thus correspond to an activity of $a_{T,m} m_D \sim 4{\times}10^3$ Bq. In order to better understand the quantity necessary for the observation and quantification of D, it is interesting to only consider the elements of the cement constituting the plasma (exponent *), thus excluding the carrier gas. Considering the mean simulation, we deduce the mole and mass fractions of deuterium in the cement aerosol $x_{\mathrm{D}}{}^* = 0.0998$ and $y_{\mathrm{D}}{}^* = 0.0150$, respectively. The minimum and maximum values lead to an averaged absolute deviation from mean simulation of $\sim 15\%$ and $\sim 47\%$ for $x_{\mathrm{H}}{}^*$ and $x_{\mathrm{D}}{}^*$, respectively. This difference in precision is explained by the low quality signal-to-base ratio and the line overlapping of D_α emission. The ratio D/H varies from ~ 0.14 to ~ 0.33 with a mean value of ~ 0.26 meaning that the ratio is stable as long as the signal allows a quantification. This value is < 1 (although the cement is mixed with deuterated water). This is explained by the hydrogen initial content into the cement powder (before mixing) and the particles air exposition before resuspension and LIBS analysis. More generally, the tritium inventory of all the powders handled (0.8 g) would thus be estimated to $\sim 5 \times 10^{12}$ Bq for the mean simulation. This value appears to be way above the regulatory limit for unsealed radioactive source of tritium set to 1 GBq g^{-1} in France.

We summarize the main characteristics of the experimental campaign described in this paper in Table 7.

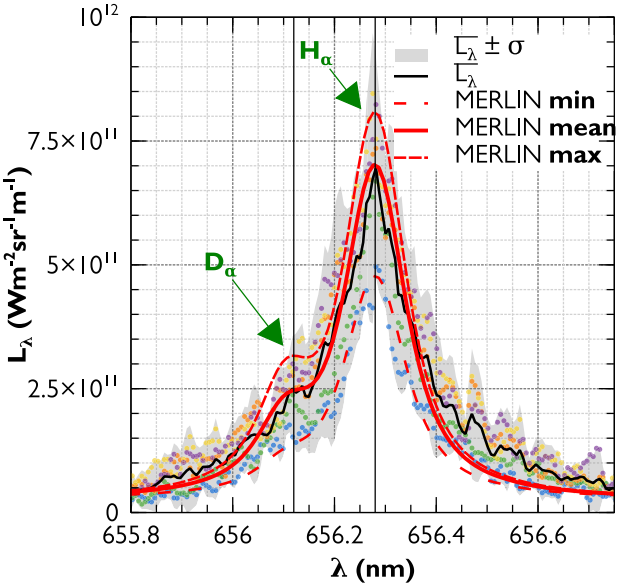

Fig. 7. Spectral radiance around H_α. The average experimental signal at $t_p = 6.5$ µs for the laser-induced plasma ($Q_t = Q_a = 4$ L min^{-1} He) on deuterated cement particles is represented by the solid black line. The corresponding standard deviation is highlighted in gray. The simulated spectra are represented in red: minimal, mean and maximal quantification are represented by long dash, solid and short dash, respectively. The corresponding D/H atomic ratio appears to be stable around ~ 0.3.

Table 7
Summary of CF-LIBS Analysis of D_2O Cement Aerosol. The digits are not indicative of the measurement precision and are provided for guidance only.

	D_2O Cement $Q_t = Q_a = 4$ L min^{-1} He
LIBS campaign date	01/2025
Sample mass (g)	0.8
φ_L (W m^{-2})	10^{17}
F_L (J cm^{-2})	10^4
τ_p (µs)	6.5
Temporal gate (ns)	100
Accumulations	100
Carrier gas	He α-gaz 2
x_{He}	0.9996799
V_p (m^3)	4.52×10^{-9}
n_e (m^{-3})	6.0×10^{21}
T (K)	12 550
p (Pa)	1.7×10^6
	Mean spectrum
$L_{\lambda=H_\alpha}$ (W m^{-2} sr^{-1} m^{-1})	6.95×10^{11}
x_H	0.0001234
$L_{\lambda=D_\alpha}$ (W m^{-2} sr^{-1} m^{-1})	2.51×10^{11}
x_D	0.0000319
$x_D{}^*$	0.0997587
$y_D{}^*$	0.0149886
m_D (in plasma, kg)	$\sim 10^{-14}$
T-equivalent activity for m_D (Bq)	4.4×10^3
T-equivalent activity for sample (Bq)	4.3×10^{12}

4. Summary and conclusions

This work demonstrates the feasibility of detecting hydrogen isotopes embedded in complex aerosol particles using calibration-free LIBS under conditions representative of nuclear decommissioning scenarios. A dedicated experimental platform was developed

to address the intrinsic challenges of aerosol LIBS, including low particle sampling rates, matrix complexity, and stringent plasma conditions required for hydrogen excitation. The robustness of the approach was validated through a reproducible resuspension protocol and consistent spectroscopic behavior, first established on alumina aerosols and subsequently applied to cement particles.

Using deuterium as a non-radioactive surrogate, we report the successful detection and quantification of isotopic signatures in airborne cement dust generated under realistic cutting conditions. Despite extremely low sampled masses, corresponding to only a few particles vaporized per acquisition, the deuterium signal could be reliably identified and modeled. The consistency between experimental spectra and CF-LIBS simulations confirms the ability to extract quantitative isotopic information in a regime dominated by discrete particle sampling and low signal-to-background ratios. In particular, the stability of the D/H ratio highlights the robustness of the method against spectral interferences and statistical fluctuations.

These results constitute a significant step towards the direct, *in situ* characterization of tritiated aerosols. They demonstrate that CF-LIBS can overcome key limitations traditionally associated with hydrogen isotope detection in complex and dilute systems. Beyond the proof of feasibility, this study establishes a methodological framework for real-time isotopic analysis of radioactive aerosols, opening perspectives for applications in nuclear safety, environmental monitoring, and future fusion facilities.

Future work should aim to improve the method's sensitivity by restricting the analysis to spectra acquired from laser-vaporized particles and by increasing the particle concentration within the LIBS interaction zone through the use of an aerosol concentrator, such as a virtual impactor. In addition, the results reported here should be further validated by investigating a wider range of D/H cement ratios and by comparing CF-LIBS quantifications with measurements obtained from complementary analytical techniques, such as thermal desorption mass spectrometry.

CRediT authorship contribution statement

Aurélien Favre: Writing – review & editing, Writing – original draft, Methodology, Investigation, Data curation, Conceptualization. **Samuel Peillon:** Writing – original draft, Investigation, Funding acquisition, Conceptualization. **Thomas Gelain:** Software. **Mickaël Payet:** Resources. **Arnaud Bultel:** Resources, Funding acquisition. **Élodie Bernard:** Resources, Funding acquisition.

Declaration of competing interest

The authors declare that they have no known competing financial interests or personal relationships that could have appeared to influence the work reported in this paper.

Acknowledgments

We are grateful to Dr. Sophie Nowak (Université Paris Cité, CNRS, ITODYS, UMR-7086) for the XRF analysis of the cement powder sample. We thank the TITANS project funded by the Euratom Research and Training Programme 2014–2018 under grant agreement No 754586. This work has been carried out within the framework of the French Federation for Magnetic Fusion Studies (FR-FCM) and of the Eurofusion consortium, and has received funding from the Euratom research and training programme 2014–2018 and 2019–2020 under grant agreement No 633053. The views and opinions expressed herein do not necessarily reflect those of the European Commission. We also thank the *Agence Nationale de la Recherche* (ANR), through the program "*Investissement d'Avenir*" (ANR-10-LABX-09-01), LabEx EMC 3, PICOLIBS project and through the program "*Investissement d'Avenir*" (ANR-10-LABX-09-01), LabEx EMC 3, PTOLEMEE project. This work has been also partially financed by the "Region Normandie", France and the European Regional Development Fund (ERDF) of the European Union, ZEOMETHYL project. Views and opinions expressed are however those of the author(s) only and do not necessarily reflect those of the European Union or the European Atomic Energy Community ('EC-Euratom'). Neither the European Union nor the granting authority can be held responsible for them.

Data availability

Data will be made available on request.

References

Almaviva, S., Caneve, L., Colao, F., Maddaluno, G., & Fantoni, R. (2021). Spectrochimica acta part b : Atomic spectroscopy accessory laboratory measurements to support quantification of hydrogen isotopes by in-situ LIBS from a robotic arm inside a fusion vessel. *Spectrochimica Acta Part B: Atomic Spectroscopy*, *181*, Article 106230. http://dx.doi.org/10.1016/j.sab.2021.106230.

Asgill, M. E., Groh, S., Niemax, K., & Hahn, D. W. (2015). The use of multi-element aerosol particles for determining temporal variations in temperature and electron density in laser-induced plasmas in support of quantitative laser-induced breakdown spectroscopy. *Spectrochimica Acta Part B: Atomic Spectroscopy*, *109*, 1–7. http://dx.doi.org/10.1016/j.sab.2015.04.005, URL: https://www.sciencedirect.com/science/article/pii/S0584854715001032.

Ashikawa, N., Torikai, Y., Asakura, N., Otsuka, T., Widdowson, A., Rubel, M., Oyaizu, M., Hara, M., Masuzaki, S., Isobe, K., Hatano, Y., Heinola, K., Baron-Wiechec, A., Jachmich, S., & Hayashi, T. (2020). Determination of retained tritium from ILW dust particles in JET. *Nuclear Materials and Energy*, *22*, Article 100673. http://dx.doi.org/10.1016/j.nme.2019.100673, URL: https://linkinghub.elsevier.com/retrieve/pii/S2352179118302849.

Bernard, E., Jambon, F., Georges, I., Sanles Sobrido, M., Rose, J., Herlin-Boime, N., Miserque, F., Beaunier, P., Vrel, D., Dine, S., Hodille, E., Chêne, J., Garcia-Argote, S., Pieters, G., Peillon, S., Gensdarmes, F., Dinescu, G., Acsente, T., Uboldi, C., ... Grisolia, C. (2019). Design of model tokamak particles for future toxicity studies: Morphology and physical characterization. *Fusion Engineering and Design*, *145*, 60–65. http://dx.doi.org/10.1016/j.fusengdes.2019.05.037, URL: https://linkinghub.elsevier.com/retrieve/pii/S0920379619306829.

Bernard, E., Sakamoto, R., Hodille, E., Kreter, A., Autissier, E., Barthe, M.-F., Desgardin, P., Schwarz-Selinger, T., Burwitz, V., Feuillastre, S., Garcia-Argote, S., Pieters, G., Rousseau, B., Ialovega, M., Bisson, R., Ghiorghiu, F., Corr, C., Thompson, M., Doerner, R., ... Grisolia, C. (2019). Tritium retention in W plasma-facing materials: Impact of the material structure and helium irradiation. *Nuclear Materials and Energy*, *19*, 403–410. http://dx.doi.org/10.1016/j.nme.2019.03.005, URL: https://linkinghub.elsevier.com/retrieve/pii/S2352179118302424.

Boudhib, M., Hermann, J., & Dutouquet, C. (2016). Compositional Analysis of Aerosols Using Calibration-Free Laser-Induced Breakdown Spectroscopy. *Analytical Chemistry*, *88*(7), 4029–4035. http://dx.doi.org/10.1021/acs.analchem.6b00329, URL: https://pubs.acs.org/doi/10.1021/acs.analchem.6b00329.

Bukki-Deme, A., Alecu, C., Kloppe, B., & Bornschein, B. (2013). First results with the upgraded TLK tritium calorimeter IGC-V0.5. *Fusion Engineering and Design*, *88*, 2865–2869. http://dx.doi.org/10.1016/j.fusengdes.2013.05.066.

Burger, M., & Hermann, J. (2016). Stark broadening measurements in plasmas produced by laser ablation of hydrogen containing compounds. *Spectrochimica Acta Part B: Atomic Spectroscopy*, *122*, 118–126. http://dx.doi.org/10.1016/j.sab.2016.06.005, URL: https://www.sciencedirect.com/science/article/pii/S0584854716300908.

Büscher, S., Wrubel, T., Ferri, S., & Kunze, H.-J. (2002). The stark width and shift of the hydrogen Hα line. *Journal of Physics B (Atomic, Molecular and Optical Physics)*, *35*(13), 2889. http://dx.doi.org/10.1088/0953-4075/35/13/304.

Cirisan, M., Cvejic, M., Gavrilovic, M., Jovicevic, S., Konjevic, N., & Hermann, J. (2014). Stark broadening measurement of Al II lines in a laser-induced plasma. *Journal of Quantitative Spectroscopy Tranfer*, *133*, 652–662. http://dx.doi.org/10.1016/j.jqsrt.2013.10.002.

Cristoforetti, G., Giacomo, A. D., Dell'Aglio, M., Legnaioli, S., Tognoni, E., Palleschi, V., & Omenetto, N. (2010). Local thermodynamic equilibrium in laser-induced breakdown spectroscopy: Beyond the McWhirter criterion. *Spectrochimica Acta - Part B Atomic Spectroscopy*, *65*, 86–95. http://dx.doi.org/10.1016/j.sab.2009.11.005.

Dalyander, P., Gornushkin, I., & Hahn, D. (2008). Numerical simulation of laser-induced breakdown spectroscopy: Modeling of aerosol analysis with finite diffusion and vaporization effects. *Spectrochimica Acta Part B: Atomic Spectroscopy*, *63*(2), 293–304. http://dx.doi.org/10.1016/j.sab.2007.11.023, URL: https://www.sciencedirect.com/science/article/pii/S0584854707004363, Honoring Issue A Collection of Papers on Atomic, Molecular and Laser Spectroscopy Dedicated to James D. Winefordner.

Diaz, D., & Hahn, D. W. (2021). Aerosol measurements with laser-induced breakdown spectroscopy and conditional analysis. *Spectrochimica Acta Part B: Atomic Spectroscopy*, *179*, Article 106107. http://dx.doi.org/10.1016/j.sab.2021.106107, URL: https://www.sciencedirect.com/science/article/pii/S0584854721000525.

Diwakar, P., Jackson, P., & Hahn, D. (2007). The effect of multi-component aerosol particles on quantitative laser-induced breakdown spectroscopy: Consideration of localized matrix effects. *Spectrochimica Acta Part B: Atomic Spectroscopy*, *62*(12), 1466–1474. http://dx.doi.org/10.1016/j.sab.2007.10.001, URL: https://www.sciencedirect.com/science/article/pii/S058485470700314X, A Collection of Papers Presented at the 4th International Conference on Laser Induced Plasma Spectroscopy and Applications (LIBS 2006).

Diwakar, P. K., Loper, K. H., Matiaske, A. M., & Hahn, D. W. (2012). Laser-induced breakdown spectroscopy for analysis of micro and nanoparticles. *Journal of Analytical Atomic Spectrometry*, *27*(7), 1110. http://dx.doi.org/10.1039/c2ja30012e, URL: https://xlink.rsc.org/?DOI=c2ja30012e.

D'Ulivo, A., Onor, M., Pitzalis, E., Spiniello, R., Lampugnani, L., Cristoforetti, G., Legnaioli, S., Palleschi, V., Salvetti, A., & Tognoni, E. (2006). Determination of the deuterium/hydrogen ratio in gas reaction products by laser-induced breakdown spectroscopy. *Spectrochimica Acta - Part B Atomic Spectroscopy*, *61*, 797–802. http://dx.doi.org/10.1016/j.sab.2006.06.001.

El-Kharbachi, A., Chêne, J., Garcia-Argote, S., Marchetti, L., Martin, F., Miserque, F., Vrel, D., Redolfi, M., Malard, V., Grisolia, C., & Rousseau, B. (2014). Tritium absorption/desorption in ITER-like tungsten particles. *International Journal of Hydrogen Energy*, *39*(20), 10525–10536. http://dx.doi.org/10.1016/j.ijhydene.2014.05.023, URL: https://linkinghub.elsevier.com/retrieve/pii/S0360319914013275.

Evans, C. J., & Gamal, Y. E. E. D. (1980). Laser-induced breakdown of helium. *Journal of Physics D (Applied Physics)*, *13*(8), 1447. http://dx.doi.org/10.1088/0022-3727/13/8/014.

Fantoni, R., Almaviva, S., Caneve, L., Colao, F., Maddaluno, G., Gasior, P., & Kubkowska, M. (2017). Hydrogen isotope detection in metal matrix using double-pulse laser-induced breakdown-spectroscopy. *Spectrochimica Acta Part B*, *129*, 8–13. http://dx.doi.org/10.1016/j.sab.2016.12.008.

Favre, A., Abad, A., Poux, A., Gosse, L., Berjaoui, A., Morel, V., & Bultel, A. (2025). Towards real-time calibration-free LIBS supported by machine learning. *Spectrochimica Acta Part B: Atomic Spectroscopy*, *224*, Article 107082. http://dx.doi.org/10.1016/j.sab.2024.107082, URL: https://linkinghub.elsevier.com/retrieve/pii/S0584854724002271.

Favre, A., Bultel, A., Morel, V., Lesage, M., & Gosse, L. (2025). MERLIN, an adaptative LTE radiative transfer model for any mixture: Validation on Eurofer97 in argon atmosphere. *Journal of Quantitative Spectroscopy and Radiative Transfer*, *330*, Article 109222. http://dx.doi.org/10.1016/j.jqsrt.2024.109222, URL: https://linkinghub.elsevier.com/retrieve/pii/S0022407324003297.

Favre, A., Bultel, A., Payet, M., Vartanian, S., Garcia-Argote, S., Morel, V., Bernard, E., Markelj, S., Čekada, M., Hodille, E., Semerok, A., & Grisolia, C. (2024). LIBS analysis of tritium in thin film-type samples. *Journal of Nuclear Materials*, *591*, Article 154924. http://dx.doi.org/10.1016/j.jnucmat.2024.154924, URL: https://linkinghub.elsevier.com/retrieve/pii/S0022311524000291.

Gallou, G., Sirven, J. B., Dutouquet, C., Bihan, O. L., & Frejafon, E. (2011). Aerosols Analysis by LIBS for Monitoring of Air Pollution by Industrial Sources. *Aerosol Science and Technology*, *45*(8), 918–926. http://dx.doi.org/10.1080/02786826.2011.566899, URL: http://www.tandfonline.com/doi/abs/10.1080/02786826.2011.566899.

Gosse, L., Favre, A., Bultel, A., Morel, V., Djurović, S., Simić, N., & Gavanski, L. (2025). In-depth stark broadening study of neutral oxygen 777 nm triplet. *Spectrochimica Acta Part B*, *230*, Article 107222. http://dx.doi.org/10.1016/j.sab.2025.107222.

Grisolia, C., Gensdarmes, F., Peillon, S., Dougniaux, G., Bernard, E., Autricque, A., Pieters, G., Rousseau, B., Feuillastre, S., Garcia-Argote, S., Carvalho, O., Malard, V., George, I., Lebaron-Jacobs, L., Orsiere, T., Uboldi, C., Rose, J., Sanles Sobrido, M., Lambertin, D., ... Dinescu, G. (2019). Current investigations on tritiated dust and its impact on tokamak safety. *Nuclear Fusion*, *59*(8), Article 086061. http://dx.doi.org/10.1088/1741-4326/ab1a76, URL: https://iopscience.iop.org/article/10.1088/1741-4326/ab1a76.

Hahn, D. (1998). Laser-induced breakdown spectroscopy for sizing and elemental analysis of discrete aerosol particles. *Applied Physics Letters*, *72*(23), 2960–2962. http://dx.doi.org/10.1063/1.121507, URL: https://pubs.aip.org/apl/article/72/23/2960/68995/Laser-induced-breakdown-spectroscopy-for-sizing.

Hahn, D., Flower, W., & Hencken, K. (1997). Discrete particle detection and metal emissions monitoring using laser-induced breakdown spectroscopy. *Applied Spectroscopy*, *51*(12), 1836–1844. http://dx.doi.org/10.1366/0003702971939659, URL: https://journals.sagepub.com/doi/10.1366/0003702971939659.

Hahn, D. W., & Lunden, M. M. (2000). Detection and Analysis of Aerosol Particles by Laser-Induced Breakdown Spectroscopy. *Aerosol Science and Technology*, *33*(1–2), 30–48. http://dx.doi.org/10.1080/027868200410831, URL: http://www.tandfonline.com/doi/abs/10.1080/027868200410831.

Hu, Z., Zhang, D., Wang, W., Chen, F., Xu, Y., Nie, J., Chu, Y., & Guo, L. (2022). A review of calibration-free laser-induced breakdown spectroscopy. *TRAC Trends in Analytical Chemistry*, *152*, Article 116618. http://dx.doi.org/10.1016/j.trac.2022.116618, URL: https://linkinghub.elsevier.com/retrieve/pii/S0165993622001017.

Kim, T. K., Lim, J., Lee, M., Yoo, J., & Grandy, C. (2021). Assessment of tritium effluent from Prototype Generation IV Sodium-cooled Fast Reactor. *Annals of Nuclear Energy*, *159*, Article 108334. http://dx.doi.org/10.1016/j.anucene.2021.108334, URL: https://linkinghub.elsevier.com/retrieve/pii/S0306454921002103.

Konjević, N., Ivković, M., & Sakan, N. (2012). Hydrogen balmer lines for low electron number density plasma diagnostics. *Spectrochimica Acta - Part B Atomic Spectroscopy*, *76*, 16–26. http://dx.doi.org/10.1016/j.sab.2012.06.026.

Konjevic, N., Lesage, A., Fuhr, J., & Wiese, W. (2002). Experimental stark widths and shifts for spectral lines of neutral and ionized atoms (A critical review of selected data for the period 1989 through 2000). *Journal of Physical and Chemical Reference Data*, *31*, 819–927. http://dx.doi.org/10.1063/1.1486456.

Kramida, A., Ralchenko, Y., Reader, J., & NIST ASD Team (2024) (2025). *NIST atomic spectra database (version 5.12), [Online]*. Gaithersburg, MD: National Institute of Standards and Technology, http://dx.doi.org/10.18434/T4W30F, URL: https://physics.nist.gov/asd.

Lee, H., Jeong, Y. S., Choi, K., & Shin, W. G. (2017). The effect of sheath flow rate on the particle trajectory inside an optical cavity with direct flow configuration. *Journal of Aerosol Science*, *114*, 146–156. http://dx.doi.org/10.1016/j.jaerosci.2017.09.016, URL: https://linkinghub.elsevier.com/retrieve/pii/S0021850217301751.

Liu, S., Zhang, Y., Feng, J., Gao, W., Li, T., & Liu, Y. (2026). Atmospheric carbon concentration scenario classification based on the fusion of spectral and acoustic modalities. *Optics Letters*, *51*(4), 949–952. http://dx.doi.org/10.1364/OL.576900, URL: https://opg.optica.org/ol/abstract.cfm?URI=ol-51-4-949.

Marina-Montes, C., Motto-Ros, V., Pérez-Arribas, L. V., Anzano, J., Millán-Martínez, M., & Cáceres, J. O. (2021). Aerosol analysis by micro laser-induced breakdown spectroscopy: A new protocol for particulate matter characterization in filters. *Analytica Chimica Acta*, *1181*, Article 338947. http://dx.doi.org/10.1016/j.aca.2021.338947, URL: https://linkinghub.elsevier.com/retrieve/pii/S000326702100773X.

Matsuyama, M., & Abe, S. (2016). Tracking of tritium charged into stainless steel by BIXS. *Fusion Engineering and Design*, *113*, 250–254. http://dx.doi.org/10.1016/j.fusengdes.2016.08.013.

Mijatovic, Z., Djurovic, S., Gavanski, L., Gajo, T., Favre, A., Morel, V., & Bultel, A. (2020). Plasma density determination by using hydrogen balmer h_α spectral line with improved accuracy. *Spectrochimica Acta Part B*, *166*, Article 105821. http://dx.doi.org/10.1016/j.sab.2020.105821.

Morgan, F., Evans, L. R., & Morgan, C. G. (1971). Laser beam induced breakdown in helium and argon. *Journal of Physics D (Applied Physics)*, *4*(2), 225. http://dx.doi.org/10.1088/0022-3727/4/2/307.

Otsuka, T., Masuzaki, S., Ashikawa, N., Hatano, Y., Asakura, Y., Suzuki, T., Suzuki, T., Isobe, K., Hayashi, T., Tokitani, M., Oya, Y., Hamaguchi, D., Kurotaki, H., Sakamoto, R., Tanigawa, H., Nakamichi, M., Widdowson, A., & Rubel, M. (2018). Tritium retention characteristics in dust particles in JET with ITER-like wall. *Nuclear Materials and Energy*, *17*, 279–283. http://dx.doi.org/10.1016/j.nme.2018.11.001, URL: https://linkinghub.elsevier.com/retrieve/pii/S2352179118301431.

Parigger, C. G., Surmick, D. M., Gautam, G., & Sherbini, A. M. E. (2015). Hydrogen alpha laser ablation plasma diagnostics. *Optics Letters*, *40*, 3436. http://dx.doi.org/10.1364/ol.40.003436.

Paris, P., Butikova, J., Laan, M., Aints, M., Hakola, A., Piip, K., Tufail, I., & Veis, P. (2017). Detection of deuterium retention by LIBS at different background pressures. *Physica Scripta*, *2017*, http://dx.doi.org/10.1088/0031-8949/2017/T170/014003.

Park, K., Cho, G., & Kwak, J. h. (2009). Development of an Aerosol Focusing-Laser Induced Breakdown Spectroscopy (Aerosol Focusing-LIBS) for Determination of Fine and Ultrafine Metal Aerosols. *Aerosol Science and Technology*, *43*(5), 375–386. http://dx.doi.org/10.1080/02786820802662947, URL: http://www.tandfonline.com/doi/abs/10.1080/02786820802662947.

Peillon, S., Dougniaux, G., Payet, M., Bernard, E., Pieters, G., Feuillastre Ressources, S., Garcia-Argote, S., Gensdarmes, F., Arnas, C., Miserque, F., Herlin-Boime, N., Grisolia, C., & Pluchery, O. (2020). Dust sampling in WEST and tritium retention in tokamak-relevant tungsten particles. *Nuclear Materials and Energy*, Article 100781. http://dx.doi.org/10.1016/j.nme.2020.100781, URL: http://www.sciencedirect.com/science/article/pii/S2352179120300570.

Roldán, A. M., Dwivedi, V., Veis, M., Atikukke, S., Meiden, H. V. D., Držík, M., & Veis, P. (2021). Quantification of hydrogen isotopes by CF-LIBS in a W-based material (WZr) at atmospheric pressure: From ns towards ps. *Physica Scripta*, *96*, http://dx.doi.org/10.1088/1402-4896/ac35f2.

Roynette, A., & Gensdarmes, F. (2012). Device for generating an aerosol with a controlled particle size. EP2794117B1.

Sharpe, M., Fagan, C., & Shmayda, W. T. (2019). Distribution of Tritium in the Near Surface of Type 316 Stainless Steel. *Fusion Science and Technology*, *75*(8), 1053–1057. http://dx.doi.org/10.1080/15361055.2019.1644136, URL: https://www.tandfonline.com/doi/full/10.1080/15361055.2019.1644136.

Sherbini, A. M. E., Aamer, A. A. S. A., Hassan, A. T., & Sherbini, T. M. E. (2012). Measurements of plasma electron temperature utilizing magnesium lines appeared in laser produced aluminum plasma in air. *Optics and Photonics Journal*, *02*, 278–285. http://dx.doi.org/10.4236/opj.2012.24034.

Slomberg, D. L., Auffan, M., Payet, M., Carboni, A., Ouaksel, A., Brousset, L., Angeletti, B., Grisolia, C., Thiéry, A., & Rose, J. (2024). Tritiated stainless steel (nano)particle release following a nuclear dismantling incident scenario: Significant exposure of freshwater ecosystem benthic zone. *Journal of Hazardous Materials*, *465*, Article 133093. http://dx.doi.org/10.1016/j.jhazmat.2023.133093, URL: https://linkinghub.elsevier.com/retrieve/pii/S0304389423023774.

Turcu, I., Gower, M., & Huntington, P. (1997). Measurement of KrF laser breakdown threshold in gases. *Optics Communications*, *134*(1), 66–68. http://dx.doi.org/10.1016/S0030-4018(96)00543-3, URL: https://www.sciencedirect.com/science/article/pii/S0030401896005433.

Vankrunkelsven, A., Dylst, K., & D'Joos, Y. (2025). Tritium Release During Different Decommissioning Techniques. *Fusion Science and Technology*, *81*(4), 294–299. http://dx.doi.org/10.1080/15361055.2024.2361198, URL: https://www.tandfonline.com/doi/full/10.1080/15361055.2024.2361198.

Vasilatou, K., Iida, K., Kazemimanesh, M., Olfert, J., Sakurai, H., Sipkens, T. A., & Smallwood, G. J. (2025). Aerosol physical characterization: A review on the current state of aerosol documentary standards and calibration strategies. *Journal of Aerosol Science*, *183*, Article 106483. http://dx.doi.org/10.1016/j.jaerosci.2024.106483, URL: https://linkinghub.elsevier.com/retrieve/pii/S0021850224001502.

Xue, B., Wang, Z., Zhu, T., Gu, Y., Sun, W., Chen, C., Li, Z., Riedel, J., & You, Y. (2024). High repetition-rate laser-induced breakdown spectroscopy combined with two-dimensional correlation method for analysis of sea-salt aerosols. *Spectrochimica Acta Part B: Atomic Spectroscopy*, *221*, Article 107048. http://dx.doi.org/10.1016/j.sab.2024.107048, URL: https://linkinghub.elsevier.com/retrieve/pii/S0584854724001927.

Ye, Y., Chen, G., Li, J., Wang, Z., Sun, Z., Aizezi, N., Deng, L., & Liu, Y. (2026). Physics-aware adaptive gated fusion for robust industrial smoke monitoring via acoustic-optical multimodal LIBS. *Optics Letters*, *51*(7), 1991–1994. http://dx.doi.org/10.1364/OL.591635, URL: https://opg.optica.org/ol/abstract.cfm?URI=ol-51-7-1991.